Neuro-Oncology Advances

5(1), 1–12, 2023 | https://doi.org/10.1093/noajnl/vdad136 | Advance Access date 18 October 2023

Radiomic features define risk and are linked to DNA methylation attributes in primary CNS lymphoma

Karl-Heinz Nenning, Johanna Gesperger, Julia Furtner, Amelie Nemc, Thomas Roetzer-Pejrimovsky, Seung-Won Choi, Christian Mitter, Stefan L. Leber, Johannes Hofmanninger, Johanna Klughammer, Bekir Ergüner, Marlies Bauer, Martina Brada, Kyuha Chong, Tanisa Brandner-Kokalj, Christian F. Freyschlag, Astrid Grams, Johannes Haybaeck, Selma Hoenigschnabl, Markus Hoffermann, Sarah Iglseder, Barbara Kiesel, Melitta Kitzwoegerer, Waltraud Kleindienst, Franz Marhold, Patrizia Moser, Stefan Oberndorfer, Daniel Pinggera, Florian Scheichel, Camillo Sherif, Guenther Stockhammer, Martin Stultschnig, Claudius Thomé, Johannes Trenkler, Tadeja Urbanic-Purkart, Serge Weis, Georg Widhalm, Franz Wuertz, Matthias Preusser, Bernhard Baumann, Ingrid Simonitsch-Klupp, Do-Hyun Nam, Christoph Bock†, , Georg Langs†, and Adelheid Woehrer†

Department of Biomedical Imaging and Image-guided Therapy, Computational Imaging Research Laboratory, Medical University of Vienna, Vienna, Austria (K.H.N., J.H., G.L.); Center for Biomedical Imaging and Neuromodulation, Nathan Kline Institute, Orangeburg, New York, USA (K.H.N.); Division of Neuropathology and Neurochemistry, Department of Neurology, Medical University of Vienna, Vienna, Austria (J.G., T.R.P., A.W.); Comprehensive Center for Clinical Neurosciences and Mental Health, Medical University of Vienna, Vienna, Austria (J.G., T.R.P., A.W.); Division of Neuroradiology, Department of Biomedical Imaging and Image-guided Therapy, Medical University of Vienna, Vienna, Austria (J.F., C.M.); Research Center for Medical Image Analysis and Artificial Intelligence (MIAAI), Faculty of Medicine and Dentistry, Danube Private University, Krems, Austria (J.F.); CeMM Research Center for Molecular Medicine of the Austrian Academy of Sciences, Vienna, Austria (A.N., J.K., B.E., C.B.); Department of Neurosurgery, Samsung Medical Center, Sungkyunkwan University School of Medicine, Seoul, Korea (S.W.C., K.C., D.H.N.); Division of Neuroradiology, Vascular, and Interventional Radiology, Department of Radiology, Medical University of Graz, Graz, Austria (S.L.L.); Department of Biochemistry, Gene Center, Ludwig-Maximilians-University, München, Germany (J.K.); Department of Neurosurgery, Medical University of Innsbruck, Innsbruck, Austria (M.B., C.F.F., P.M., D.P., C.T.); Department of Pathology, Innpath, Tirolkliniken, Innsbruck, Austria (P.M.); Department of Pathology, Klinik Landstraße, Vienna, Austria (M.B.); Institute of Pathology, State Hospital Klagenfurt, Klagenfurt, Austria (T.B.K., F.W.); Department of Neuroradiology, Medical University of Innsbruck, Innsbruck, Austria (A.G.); Institute of Pathology, Neuropathology and Molecular Pathology, Medical University of Innsbruck, Innsbruck, Austria (J.H.); Center for Molecular Biomedicine, Institute of Pathology, Medical University of Graz, Diagnostic and Research, Graz, Austria (J.H.); Department of Pathology, Donauspital Vienna, Vienna, Austria (S.H.); Department of Neurosurgery, State Hospital Feldkirch, Feldkirch, Austria (M.H.); Department of Neurology, Medical University of Innsbruck, Innsbruck, Austria (S.I., G.S.); Department of Neurosurgery, Medical University of Vienna, Vienna, Austria (B.K., G.W.); Department of Pathology, University Hospital St. Poelten, Karl Landsteiner University of Health Sciences, St. Poelten, Austria (M.K.); Department of Neurology, Paracelsus Medical University Salzburg, Salzburg, Austria (W.K.); Department of Neurosurgery, University Hospital St. Poelten, Karl Landsteiner University of Health Sciences, St. Poelten, Austria (F.M., F.S., C.S.); Department of Neurology, University Hospital St. Poelten, Karl Landsteiner University of Health Sciences, St. Poelten, Austria (S.O.); Department of Neurology, State Hospital Klagenfurt, Klagenfurt, Austria (M.S.); Institute of Neuroradiology, Kepler University Hospital, NeuromedCampus, Johannes Kepler University of Linz, Linz, Austria (J.T.); Department of Neurology, Medical University of Graz, Graz, Austria (T.U.P.); Division of Neuroradiology, Vascular and Interventional Radiology, Medical University of Graz, Graz, Austria (T.U.P.); Division of Neuropathology, Kepler University Hospital, NeuromedCampus, Johannes Kepler University, Linz, Austria (S.W.); Division of Oncology, Department of Internal Medicine 1, Medical University of Vienna, Vienna, Austria (M.P.); Center for Medical Physics and Biomedical Engineering, Medical University of Vienna, Vienna, Austria (B.B.); Department of Pathology, Medical University of Vienna, Vienna, Austria (I.S.K.); Institute of Artificial Intelligence, Center for Medical Data Science, Medical University of Vienna, Vienna, Austria (C.B.); Computer Science and Artificial Intelligence Laboratory, Massachusetts Institute of Technology, Cambridge, Massachusetts, USA (G.L.)

Corresponding Author: Adelheid Woehrer, MD PhD, Division of Neuropathology and Neurochemistry, Department of Neurology, Medical University of Vienna, Spitalgasse 23, 1090 Vienna, Austria (adelheid.woehrer@meduniwien.ac.at)

†Shared last authors.

Abstract

Background. The prognostic roles of clinical and laboratory markers have been exploited to model risk in patients with primary CNS lymphoma, but these approaches do not fully explain the observed variation in outcome. To date, neuroimaging or molecular information is not used. The aim of this study was to determine the utility of radiomic features to capture clinically relevant phenotypes, and to link those to molecular profiles for enhanced risk stratification.

Methods. In this retrospective study, we investigated 133 patients across 9 sites in Austria (2005–2018) and an external validation site in South Korea (44 patients, 2013–2016). We used T1-weighted contrast-enhanced MRI and an L1-norm regularized Cox proportional hazard model to derive a radiomic risk score. We integrated radiomic features with DNA methylation profiles using machine learning-based prediction, and validated the most relevant biological associations in tissues and cell lines.

Results. The radiomic risk score, consisting of 20 mostly textural features, was a strong and independent predictor of survival (multivariate hazard ratio = 6.56 [3.64–11.81]) that remained valid in the external validation cohort. Radiomic features captured gene regulatory differences such as in BCL6 binding activity, which was put forth as testable treatment target for a subset of patients.

Conclusions. The radiomic risk score was a robust and complementary predictor of survival and reflected characteristics in underlying DNA methylation patterns. Leveraging imaging phenotypes to assess risk and inform epigenetic treatment targets provides a concept on which to advance prognostic modeling and precision therapy for this aggressive cancer.

Key Points

- In primary CNS lymphoma, radiomic features capture imaging phenotypes and are associated with survival.
- Image-based phenotypic differences relate to distinct DNA methylation patterns.
- Differential gene regulation nominates key transcription factors as therapeutic targets.

Importance of the Study

To our knowledge, this is the first study to systematically evaluate radiomic features for their prognostic value in primary CNS lymphoma (PCNSL), and to derive a radiomic risk score that accurately stratifies patients according to risk. It further links the radiomic features with epigenome-wide DNA methylation, unraveling the gene regulatory basis that contributes to the observed phenotypic differences. Using this integrated approach, we nominate transcription factors as potential epigenetic treatment targets for subsets of patients. Our study demonstrates the potential of radiomic feature analysis as a clinically meaningful and noninvasive imaging marker for risk assessment in patients with PCNSL. Assessing risk and selecting epigenetic treatment based on radiomic phenotypes substantially advances prognostic modeling and precision therapy for this aggressive brain cancer.

Primary CNS lymphoma (PCNSL) is a malignant brain tumor characterized by extensive phenotypic variability. Clinical factors such as age, clinical performance, and immune status, as well as complex, adaptive treatment strategies shape the disease course of individual patients in myriad ways and entail survival times ranging from a few months to several decades. Two commonly used prognostic scoring systems, the models of the International Extranodal Lymphoma Study Group and the Memorial Sloan Kettering Cancer Center, rely on sets of clinical and laboratory markers to stratify patients into clinically useful risk groups, but do not fully explain the observed variation in survival.[1,2]

The phenotypic heterogeneity of PCNSL is in parts captured at the level of magnetic resonance imaging (MRI), where lesions vary in size, number of foci, and contrast enhancement.[3] Importantly, different MRI characteristics visualize tumor biological properties such as the disruption of the blood-brain barrier, tumor vascularity, cellularity, and eventually genetic alterations.[3] One particular approach that has substantially advanced the concept of phenotype-genotype correlations is the quantification of a large

number of radiomic image features that may be readily integrated with genome-wide molecular tumor profiles.[4]

The molecular landscape of PCNSL, specifically primary diffuse large B-cell lymphoma of the CNS (DLBCL-CNS), is characterized by a common transcriptional state that resembles early post-germinal center activated B-cells, who undergo continued somatic hypermutation driving genetic heterogeneity.[5–9] Only few studies have focused on its epigenomic dimensions such as DNA methylation at CpG sites,[10–13] which may, however, strike a balance between little transcriptional and excessive genetic variation. Moreover, in the context of hematological cancers, DNA methylation was found to refine prognostic rating, contribute information to new multiomic data integration, and identify key gene regulatory mechanisms as potential targets for epigenetic therapy.[14–20]

Limited information exists regarding the potential links between MRI phenotypes and epi-genotypes in PCNSL, hampering the development of novel, radiomic-based risk models that inform targeted treatment. To address this gap of knowledge, we profiled a large patient cohort at the radiomic and DNA methylation levels. We identified imaging-based risk groups that differ in their gene regulatory basis, proposing specific transcription factors as testable treatment targets in subsets of patients.

Materials and Methods

Patient Cohort and Resources

Patients were retrospectively selected from a population-scale cohort comprising 207 adult patients, extending a previous series.[21,22] The study was approved by the IRB of MedUni Vienna under #1861-2018 and written informed consent was obtained from all patients. Consecutive adult patients of both sexes with newly diagnosed PCNSL at 9 Austrian centers between January 2005 and December 2018 were eligible. Eight secondary CNS lymphomas, and 14 EBV-related PCNSLs were excluded. Another 2 cases with missing clinical information, MRI data, or tumor tissue were excluded (Figure 1A).

MRI data were available for 133 patients, and after quality assessment 83 cases were included (contrast-enhanced T1 with near-isotropic 1 mm resolution). As an external validation cohort, we obtained 44 MRI of patients acquired at the Samsung Medical Center, South Korea. MRI data were obtained during routine clinical work-up at different MR scanners (1.5T, 3T, Siemens, Philips, and GE). Each case had a minimum of contrast-enhanced T1-weighted (T1-ce) and either T2-weighted or fluid attenuated inversion recovery (FLAIR) images available. The T1-ce volumes had a consistently high resolution across all centers with a median voxel size of 0.9 × 0.86 × 1.2 mm. A board-certified radiologist (J.F. > 15 years of reading experience) and a neuroimaging expert (K.H.N. > 10 years of reading experience) consensually segmented the lesions into enhancing tumor, necrosis, and edema. J.F. labeled cases with presence of hemorrhage, calcification, heterogeneous contrast enhancement, or necrosis as atypical.[23–26]

In 116 patients, formalin-fixed and paraffin-embedded tissues were available, which were reviewed by a neuropathologist (A.W. > 15 years of diagnostic experience) to confirm the diagnosis of CNS DLBCL and to define regions for DNA isolation and reduced representation bisulfite sequencing (RRBS, $N = 78$), as well as the construction of

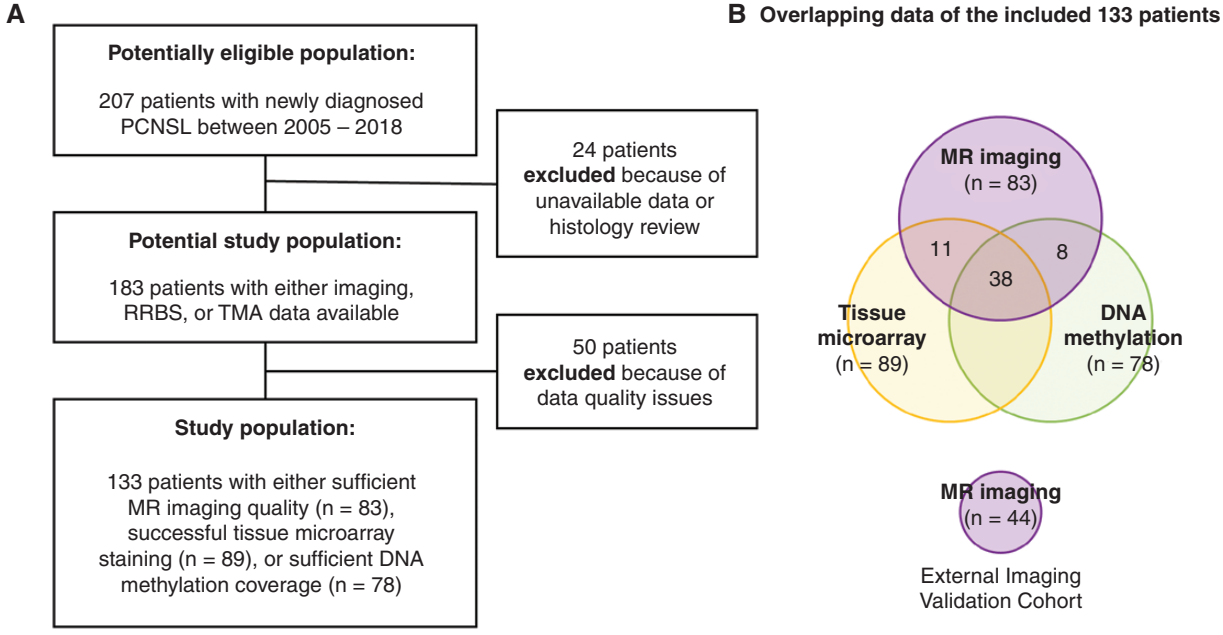

Figure 1. Overview of the study cohort and the multimodal patient annotation. (A) Flow chart of patient selection. (B) Overlapping data samples including magnetic resonance imaging (MRI) data, histology data based on tissue microarrays (TMA), and DNA methylation sequencing data.

tissue microarrays (TMA, $N = 89$). TMAs were used to allocate tumors to germinal center B-cell (GCB, 12%) or non-germinal center B-cell types (non-GCB, 88%) according to the Hans algorithm.[27]

Taken together, the discovery cohort comprised 83 cases with MRI data and 78 cases with DNA methylation profiles, with 46 cases having both (Figure 1B). Details of the multimodal workflow are provided in Supplementary Materials.

Radiomic Feature Extraction and Risk Score Generation

Radiomic features were extracted from contrast-enhanced T1-weighted MRI using the Pyradiomics library[28] and quantified for 2 tumor masks: (i) contrast-enhanced tumor and necrosis (tumor core), and (ii) contrast-enhanced tumor, necrosis, and edema (tumor-plus-vicinity). The most relevant features were identified using a least absolute shrinkage and selection operator (LASSO) with a Cox proportional hazard model implemented in Glmnet.[29] The radiomic risk score was defined as a linear combination of the coefficients of those features, and the median was used to initially stratify patients into equally sized risk groups. Feature selection and risk score generation were evaluated within the discovery cohort using 10-fold cross-validation. To exclude that the risk score was generated by chance, feature selection and risk score generation were repeated in 1,000 permutation runs with shuffled survival labels (follow-up time and survival status).

For external validation, we chose an optimal cutoff based on its discriminative performance (the highest hazard ratio (HR), lowest P value, and maximum median survival difference) in the discovery cohort. Details are provided in Supplementary Materials.

Reduced Representation Bisulfite Sequencing

Reduced representation bisulfite sequencing data were preprocessed (details see Supplementary Materials), and reads were aligned to the human reference genome (GRCh38). RRBS data analysis was restricted to gene promoter regions, and the specific DNA methylation levels were calculated with RnBeads.[30] For further analysis, we included only promoter regions that were covered in >80% of the samples, and those with <80% coverage across all promoters were excluded. Missing data were imputed with k (=5) nearest neighbors.

Integration of MRI and RRBS Data

We used a support vector machine (SVM) to predict radiomic risk groups based on DNA methylation profiles, employing 10-fold cross-validation and a permutation baseline. The receiver operating characteristic (ROC) curves and the area under the curve (AUC) were assessed for true and permuted labels. We employed locus overlap analysis (LOLA)[31] to identify group differences using the most informative sites as the LOLA universe, while restricting region sets to B-cell-related transcription factors. Their protein expression was evaluated in TMAs using immunohistochemistry (antibodies specified in Supplementary Table S1).

In Vitro Experiments

Ultimately, 2 commercially available DLBCL cell lines of ABC type with low and high BCL6 expression (NU-DHL1, OCI-LY3) were challenged with methotrexate (Sigma Aldrich, IC50) in the presence of a BCL6 inhibitor (79-6, Calbiochem, Merck KGaA, IC50) versus methotrexate alone. Experiments were performed in 3 technical replicates and repeated upon chemical degradation of BCL6 using BI-3802 (MedChem Express LLC, 3 nM). Cell viability was quantified using RealTime-Glo MT Cell Viability assays (Promega) with fluorescence read-outs at 2, 4, 19, 23, and 26 hours posttreatment. For each time point, counts of treated cells were normalized to untreated cells and the percent changes reported.

Statistical Analysis

Statistical analysis was performed with MATLAB v2014a. The primary study endpoint was overall survival. Prognostic values were assessed upon Kaplan-Meier survival analysis using logrank tests, and uni- and multivariate Cox regression with backwards elimination. P values < .05 were considered significant, and where appropriate, corrected for multiple comparisons using false discovery rate correction.

Data Availability

The RRBS data and the de-identified MRI data are available from the corresponding author upon request and after signing a data usage agreement. Radiomic features were based on the openly available Pyradiomics feature library (https://pyradiomics.readthedocs.io/). The glmnet toolbox is available at https://glmnet.stanford.edu/.

Results

A total of 133 patients fulfilled the criteria of adequate MRI ($N = 83$) and/or tumor tissue availability (RRBS in 78, TMA-based histology in 89; Figure 1B). The median age at surgery was 66 years (range 23–84 years), and the median survival time was 10.6 months. The clinical characteristics are summarized in Table 1 demographics.

Radiomic Risk Score Captures Differences in Survival

The L1-norm regularized Cox proportional hazard model identified 20 radiomic features that were consistently associated with survival (10-fold cross-validation data in Supplementary Figure S1B). The linear combination of those features resulted in a radiomic risk score, where a higher score indicated a shorter survival. A risk-score-by-feature-weight heatmap pointed toward 2 equally sized groups (Figure 2A), which were confirmed by a UMAP

Table 1. Baseline Demographic and Clinical Characteristics of 133 Patients in the Discovery Cohort and 44 Patients in the Validation Cohort

	Discovery Cohort	Validation Cohort
Sex		
Male	69 (51.9%)	25 (56.8%)
Female	64 (48.1%)	19 (43.2%)
Age, y		
Median (range)	66 (23–84)	57 (20–77)
Overall survival		
Median survival time	10.6 months	40.6 months
Tumor properties, mm^3		
Volume enhancing	mean: 17.32, std: 18.65	mean: 25.46, std: 23.57
Volume edema	mean: 92.43, std: 71.62	mean: 98.87, std: 58.55
Volume necrosis	mean: 0.35, std: 1.66	mean: 0.95, std: 3.28
Number of tumor foci		
1	54 (40.6%)	19 (43.2%)
>1	66 (49.6%)	25 (56.8%)
N/A	13 (9.8%)	—
First line treatment		
Chemotherapy (CT)	73 (54.9%)	20 (45.4%)
Radiation therapy (RT)	11 (8.3%)	1 (2.3%)
Combined CT-RT	28 (21.0%)	20 (45.4%)
Best supportive care	12 (9.0%)	1 (2.3%)
N/A	9 (6.8%)	2 (4.6%)
ECOG performance status		
0/1	72 (54.2%)	—
>1	43 (32.3%)	—
N/A	18 (13.5%)	—
Activities of daily living performance		
Independent	—	27 (61.4%)
Moderate assist	—	15 (34.0%)
Minimal assist	—	2 (4.6%)
Methotrexate		
Yes	91 (68.4%)	40 (91.0%)
No	33 (24.8%)	2 (4.5%)
N/A	9 (6.8%)	2 (4.5%)
Rituximab (375 mg/m^2)		
Yes	27 (20.3%)	4 (9.1%)
No	96 (72.2%)	38 (86.4%)
N/A	10 (7.5%)	2 (4.5%)
Median number of therapy cycles		
Methotrexate	4 (1–8)	9 (1–19)
Rituximab	3.5 (1–7)	N/A
LDH level		
Normal	71 (53.4%)	—
Elevated	29 (21.8%)	—
N/A	33 (24.8%)	—

Table 1. Continued

	Discovery Cohort	Validation Cohort
Second line treatment		
Yes	20 (15.0%)	27 (61.4%)
	HD-MTX (5), Rituximab (3), R-CHOP (2), HD-AraC (2), Topotecan (1), MTX (1), Cytarabin (1), AraC (1), N/A (4)	Ara-C (13), ICE/Dexa (6), HD Ara-C #2 (2), R-CHOP (1), HD cytarabine (1), GDP (1), FOLFOX (1), Etoposide (1), Cytarabine (1)
No	102 (76.7%)	15 (34.1%)
N/A	11 (8.3%)	2 (4.5%)
Radiation therapy details		
N/A	106 (79.7%)	44 (100%)
Completed (yes/no/n/a)	20/5/2	—
Dose (average, std)	38.85 (8.79)	—
Fractions (average, std)	1.95 (0.15)	—
Autologous stem cell transplantation		
Yes	6 (4.5%)	9 (20.5%)
No	109 (82.0%)	33 (75.0%)
N/A	18 (13.5%)	2 (4.5%)

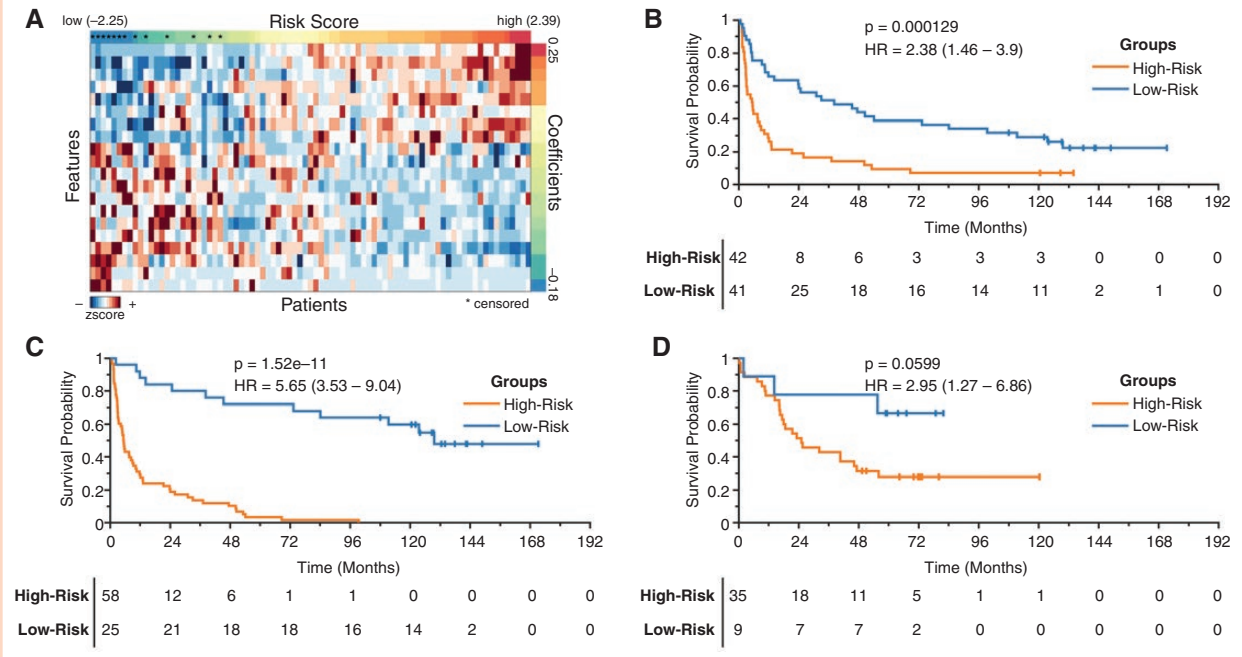

Figure 2. Radiomic risk score captures differences in survival. (A) Heatmap of patients ranked by the radiomic risk score and by the feature weights. (B) Kaplan-Meier survival analysis of the discovery cohort stratified at the median risk score, upon 10-fold cross-validation. (C) Kaplan-Meier survival analysis stratified at the cutoff with maximized hazard ratio in the discovery cohort. (D) Kaplan-Meier survival analysis stratified at the transferred cutoff in the external validation cohort.

representation of feature similarities (Supplementary Figure S1C). Splitting the cohort at the median risk score resulted in significant survival differences (Figure 2B, HR = 2.38 [1.46–3.90], median overall survival (OS): high-risk 5.3 months, low-risk 38.2 months). As a confirmation, 1,000 permutation runs repeating feature selection and risk score generation based on shuffled survival labels did not randomly result in a larger survival difference (Supplementary Figure S1D). The strictly test-only validation cohort using 44 MRIs of an independent sample differed in acquisition settings and

patient demographics (Supplementary Figure S2A). While the transfer of the median risk score as a cutoff found in the discovery cohort did not replicate survival differences in the validation cohort, a cutoff based on the maximal hazard ratio in the discovery cohort showed a trend toward survival differences in the validation cohort (Figure 2C, Supplementary Table S2; HR = 5.65 [3.53–9.04], median OS: high-risk 5.4 months, low-risk 129.6 months; Figure 2D, HR = 2.95 [1.27–6.86], median OS: high-risk 25.1 months, low-risk: not reached). However, an optimal cutoff was also found for the validation cohort, which yielded significant survival differences (Supplementary Figure S6, Supplementary Table S5; P = .013, HR 3.45 [1.6–7.44]), supporting the overall relevance and generalizability of the extracted imaging features.

Radiomic Risk Groups Differ in Clinical and MR Imaging Phenotypes

When comparing the risk score with an extended set of clinical and MRI features, a mere correlation with age was observed (ρ = 0.29, pFDR = 0.07, Figure 3A). Uni- and multivariate Cox regression analyses confirmed a strong association between survival and the radiomic risk score (univariate HR = 6.36 [3.57–11.34], Figure 3B; multivariate HR = 6.56 [3.64–11.81], Figure 3C). In the validation cohort, multivariate Cox regression yielded a sole significant association between survival and volume of necrosis (HR = 4.27 [1.81–10.05]), and the radiomic risk score was removed from the multivariate model as the second-to-last feature before the last iteration with a P value of .0636. The risk score did not differ significantly between submitting centers (ANOVA $F(8,74) = 1.8$, $P = .095$; Supplementary Figure S2B) and risk groups showed a comparable prevalence of treatment modalities (#low-risk: 53.7% CT, 21.9% CT-RT, 12.2% RT-BSC, 12.2% ASCT; #high-risk: 69.1% CT, 23.8% CT-RT, 7.1% RT-BSC; Supplementary Figure S3). Of note, it also provided a stronger association with survival than the Memorial Sloan Kettering Cancer Center (MSKCC) score (Figure 3B), which did not create independent prognostic classes in our discovery cohort (Supplementary Figure S1E). High-risk lesions preferentially involved the anterior and posterior corpus callosum, where they showed a stronger spatial overlap than low-risk lesions (Figure 3D).

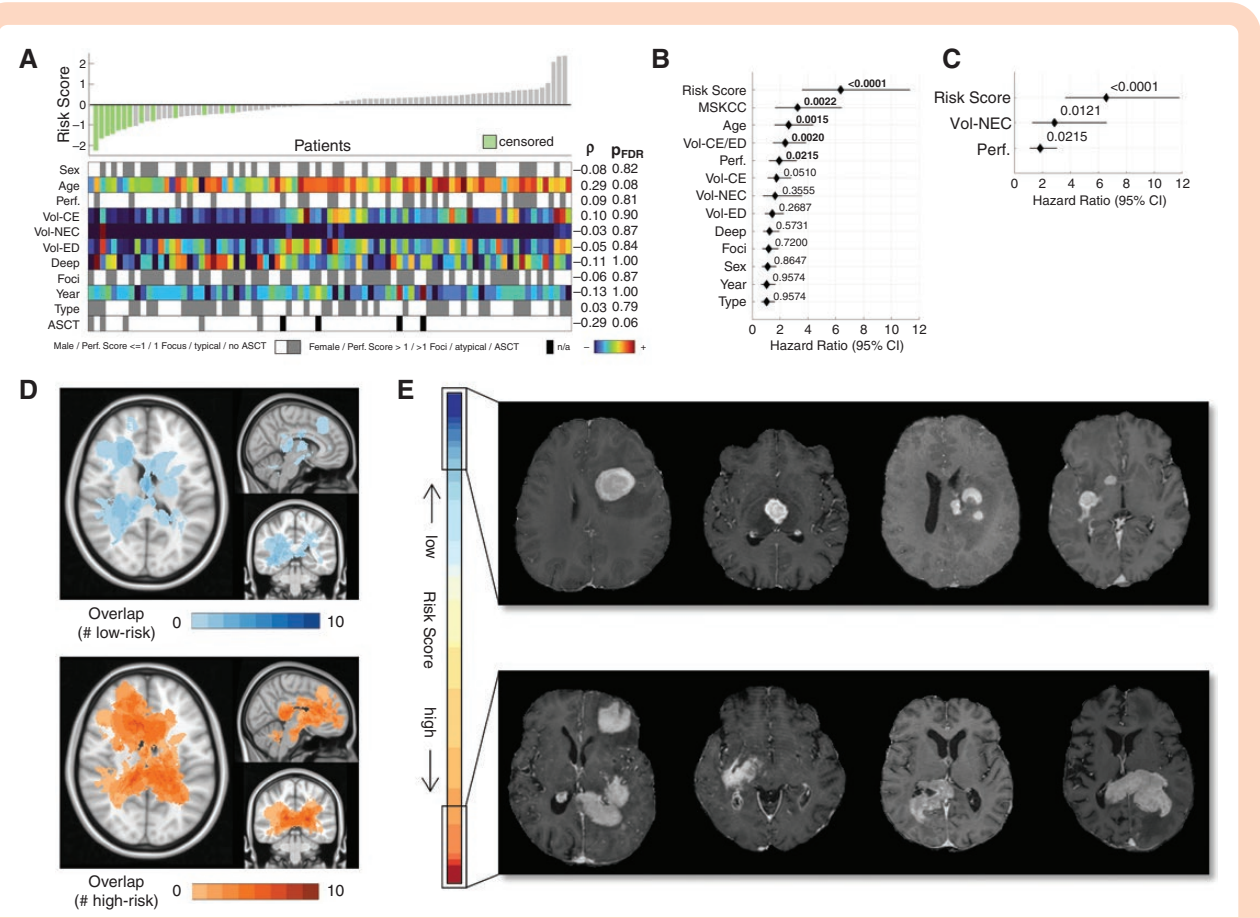

Figure 3. Radiomic risk groups differ in clinical and MR imaging phenotypes. (A) Correlation (Spearman's ρ) of the risk score with clinical and imaging parameters (Perf = clinical performance ECOG score; Vol-CE = volume contrast-enhancing tumor; Vol-NEC = volume of necrosis; Vol-ED = volume of edema; Deep = involvement of deep brain location; Foci = multifocal disease; Year = year of diagnosis; Type = typical/atypical; ACST = autologous stem cell transplantation). (B) Forest plots of univariate, and (C) multivariate Cox regression analyses (Vol-CE/ED = ratio of contrast-enhancing tumor and edema, MSKCC = Memorial Sloan Kettering Cancer Center score). (D) Degree of spatial overlap among high- and low-risk tumors. (E) Representative MRI of cases with high- and low-risk scores.

Table 2. Core Radiomic Features Included in the Risk Score. Out of the 20 Identified Features, 17 Captured Texture Characteristics and 3 Intensity (Firstorder) Profiles. No Shape Features Were Identified As Predictive

Coefficients	Labels	Type	Tissue	Wavelet	Interpretation
0.25106889	Gray level nonuniformity	glszm	Tumor core	HLH	Skewed distribution of gray-level size zones
0.18059428	Sum entropy	glcm	Core + vicinity	LLL	Neighborhood intensity value differences
0.148945719	Interquartile range	firstorder	Core + vicinity	HLL	Intensity range
0.13777253	Cluster shade	glcm	Core + vicinity	LLH	Skewness and uniformity of the GLCM
0.130139962	Small area emphasis	glszm	Tumor core	HHL	Distribution of small gray-level size zones
0.037002116	Skewness	firstorder	Core + vicinity	LHH	Asymmetry of the intensity distribution
0.033505563	Inverse variance	glcm	Tumor core	LLH	Inverse of the variance
0.015692966	Robust mean absolute deviation	firstorder	Core + vicinity	—	Mean distance of all intensity values from the mean
−0.010046394	Informational measure of correlation 2	glcm	Tumor core	LLH	Complexity of texture
−0.015986847	Maximal correlation coefficient	glcm	Tumor core	LHL	Complexity of texture
−0.0368548	Large area high gray level emphasis	glszm	Core + vicinity	LLL	Larger size zones with higher gray-level values
−0.042206768	Small area low gray level emphasis	glszm	Tumor core	—	Smaller size zones with lower gray-level values
−0.0465881	Small dependence high gray level emphasis	gldm	Tumor core	LLH	Small dependence with higher gray-level values
−0.051812131	Large area emphasis	glszm	Core + vicinity	LLL	Coarseness of texture
−0.069709197	Long run high gray level emphasis	glrlm	Core + vicinity	LLH	Joint distribution of long run lengths with higher gray-level values
−0.081066228	Contrast	glcm	Tumor core	LLH	Local intensity variation
−0.089818195	Long run emphasis	glrlm	Core + vicinity	LLL	Distribution of long run lengths
−0.132682264	Cluster shade	glcm	Tumor core	LHL	Skewness and uniformity of the GLCM
−0.14236702	Large area low gray level emphasis	glszm	Tumor core	HLH	Larger size zones with lower gray-level values
−0.182621688	Strength	ngtdm	Tumor core	LHH	Coarse differences in gray level intensities

Among the 20 selected radiomic features, 17 were texture features, emphasizing the informative value of intensity-based heterogeneity (Table 2). Similarly, the balanced selection of features derived from both masks, that is, tumor core and tumor-plus-vicinity, suggested that the relation between tumor and surroundings was important. Of note, the predictive value of the radiomic features was superior to mere volumetric differences in contrast enhancement and edema (Figure 3D), and superior to the presence of gross atypical radiologic findings (Figure 3A, $r = 0.03$, $P = .79$). Overall, low-risk tumors were characterized by ordered intensity differences such as sharper edges or ring-like structures, while high-risk tumors were characterized by patchy and ill-defined contrast enhancement (representative MRI in Figure 3E).

Radiomic Risk Groups Differ in DNA Methylation Attributes and Key Transcription Factors

A SVM-based classifier was trained on DNA methylation data to predict radiomic risk groups, which showed a good performance upon 10-fold cross-validation (AUC = 0.78, Figure 4A). A risk-score-by-weight heatmap of the 1,000 most predictive DNA methylation sites suggested more abundant DNA hypomethylation of high-risk tumors with more pronounced interpatient variability (Figure 4B), which was confirmed across genome-wide CpG sites (Figure 4C). DNA methylation loss for high-risk tumors indicated enrichment of the Wnt signaling pathway, Hedgehog signaling pathway, and synaptic vesicle trafficking pathway (Supplementary Table S3). A LOLA using the 1,000 most informative sites as a query set, found strong enrichment for BCOR, BCL6, and RUNX3 binding sites in hypermethylated regions of high-risk tumors (Figure 4D). Following up on BCL6 as a master regulator of the germinal center reaction, whose activity is sensitive to DNA methylation,[32] its diminished protein expression was confirmed in high-risk tumors (Figure 4E) independent of transcriptional subtype (Supplementary Figure S4).

To probe the computational findings in vitro, 2 ABC-type DLBCL cell lines with diverging high and low BCL6 expression levels, NU-DHL1 and OCI-LY3 (Supplementary Figure S5), were challenged with methotrexate plus the BCL6 inhibitor 79-6, which resulted in an added benefit of combined treatment in both cell lines, being more pronounced with higher BCL6 levels (Figure 4F) and reverted upon chemical BCL6 degradation (Figure 4G).

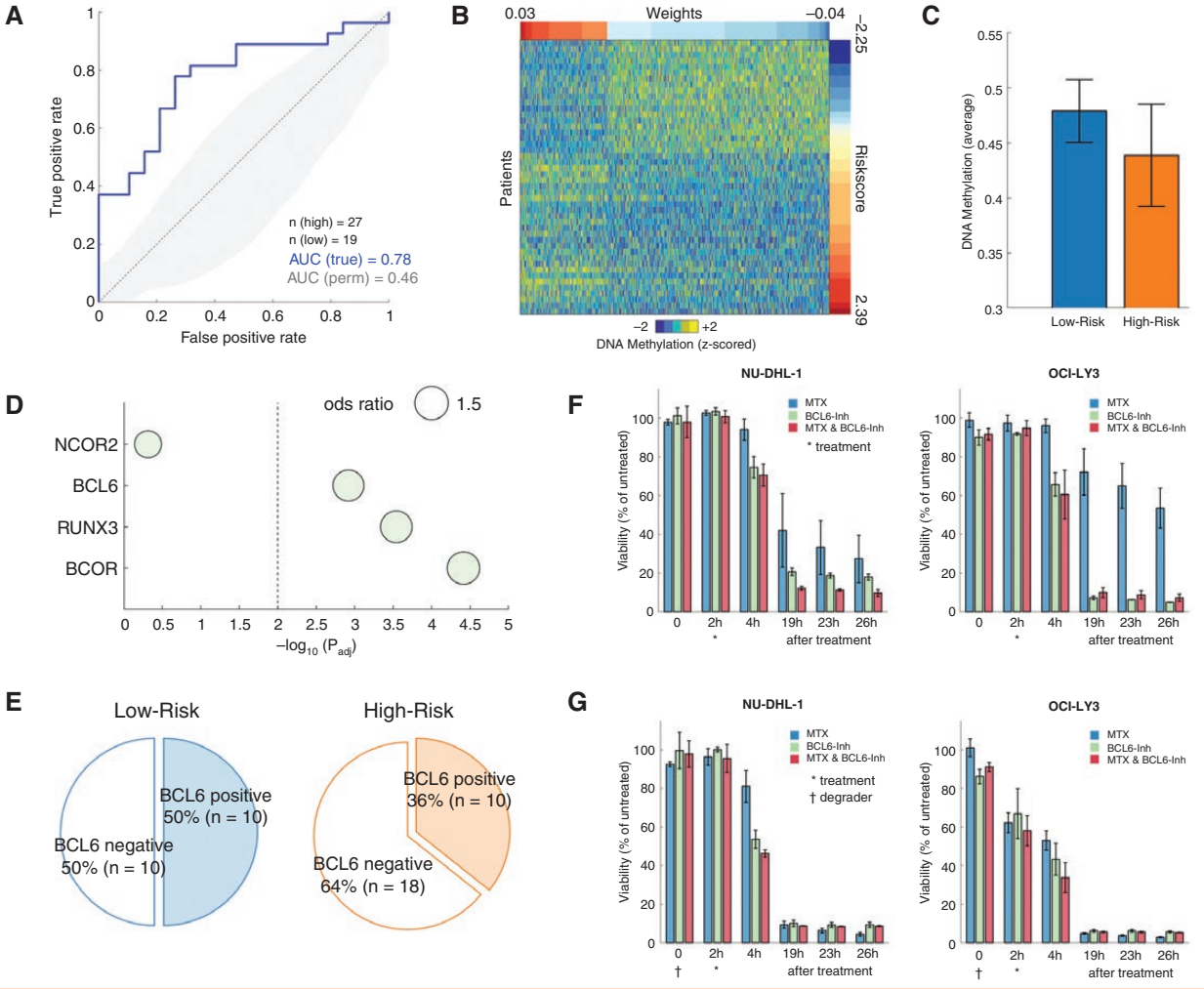

Figure 4. Radiomic risk groups differ in DNA methylation attributes and key transcription factors. (A) ROC curve of the prediction of radiomic risk groups based on DNA methylation upon 10-fold cross-validation. (B) Heatmap of the 1,000 most discriminatory DNA methylation sites. (C) Average genome-wide promoter DNA methylation levels according to risk group. Error bars indicate standard deviation. (D) Locus overlap analysis (LOLA) for hypermethylated promoters in the high-risk group. (E) BCL6 protein expression according to risk group. (F) Effects of combined treatment using methotrexate plus a BCL6 inhibitor in 2 ABC-type DLBCL cell lines. Error bars indicate standard deviation. (G) Effects of combined treatment upon prior chemical degradation of BCL6. Error bars indicate standard deviations in all subplots.

Discussion

In this study, comprising patients from 9 centers and one additional external site, we established and evaluated a novel risk score for patients with PCNSL that accurately identifies those at risk for aggressive disease and early death. The risk score is based on a set of radiomic features extracted from routinely available, preoperative contrast-enhanced T1-weighted MRI. It is noninvasive and objective, and has the potential to improve existing prognostic scoring systems. In our retrospective setting with limited availability of laboratory markers, we were able to comparatively evaluate the radiomic risk score against the MSKCC prognostic score,[2] which relies on age and clinical performance. Intriguingly, we found the risk score to be more sensitive (higher hazard ratio) upon univariate direct comparison.

Unlike previous studies that mostly cataloged radiomic features to delineate PCNSL from other tumors such as glioblastoma,[33–37] our study identified clinically relevant subgroups within PCNSL. In line with recent work, textural features were particularly informative.[35–39] Of note, in the present cohort, the tumor surroundings contributed relevant information to the model, which is important to consider since those regions are not necessarily included in radiomic studies.[40–42] Moreover, we evaluated the radiomic risk score in a multicenter setting across different MRI scanning conditions and distinct patient populations, suggesting resilience and generalizability of informative imaging-based features in patients with PCNSL. Its continued evaluation in prospective series, also incorporating novel therapies with prolonged survival will be key to further substantiate its prognostic rating ability. Along this line, prospective cohorts will be best suited to further

develop it, for example, through the inclusion of additional MRI sequences and/or longitudinal imaging data.

Mining imaging features at scale, and linking them to epigenetic profiles allowed us to identify key transcription factors as potential treatment targets that may advance tailored treatment strategies. Precisely, gene regulatory differences underlying the radiomic risk groups nominated 3 key transcription factors including BCL6. We provided experimental data corroborating the latter, since biologically it acts in tandem with BCOR and had been previously shown to be regulated by DNA methylation, even though its prognostic role is controversially discussed in PCNSL.[43,44] Of note, multiomic data integration further supported a role for DNA hypermethylation and differential BCL6 binding activity in defining distinct clusters of PCNSL that were associated with immune cold tumor microenvironments.[20] Our in vitro experiments suggested some antitumor activity of BCL6 inhibition when combined with methotrexate, in line with a recent report.[45] Beyond BCL6 as a potential target, our study highlights the potential of leveraging imaging phenotypes to allocate patients to targeted treatments in future clinical trials.

Our study has several limitations. First, larger prospective series will be needed to define and specify an optimal risk score cutoff prior to its integration in prognostic scoring systems such as the MSKCC prognostic score[2] or newer refined versions that integrate lactate dehydrogenase-to-lymphocyte ratio.[46] Second, the external replication cohort provided by a tertiary care center, differed in terms of better overall survival, younger patient age, and larger tumor size, but still supported the generalizability of the selected radiomic features. Third, our samples lacked anatomical annotation, which prevented a more precise phenotype-epigenotype correlation. Even though the majority of our samples were likely derived from contrast-enhancing tumor regions (as prime target during neurosurgery), at the histological level a fraction also displayed adjacent brain parenchyma and/or tumor necrosis. Hence, future approaches will benefit from the exact coregistration. Similarly, information on prior cortisol treatment would be relevant because of its rapid tumor-vanishing effect. However, high tumor cell densities and retained diagnostic features of all biopsies suggested minor effects in the present series. Ultimately, it would have been desirable to evaluate drug response directly in PCNSL-derived cell lines (ideally with matched MRI data), which was hampered by the lack of well-characterized and commercially available cell lines. This seems particularly important given the multifaceted role of BCL6 in B-cells during adaptive immunity, and the need for its further investigation in PCNSL patients and patient-derived cells.

In summary, we present a radiomics-based risk score that accurately predicts survival for patients with PCNSL and informs biological differences that underlie the radiomically defined groups. Differences in master gene regulatory programs converged on BCL6 activity as testable therapeutic intervention. From the perspective of precision medicine, assessing risk and selecting targeted treatment based on objective MRI criteria represents an important step forward, and the radiomic risk groups provide a promising basis for developing personalized therapy for this aggressive brain cancer.

Supplementary material

Supplementary material is available online at *Neuro-Oncology* (https://academic.oup.com/neuro-oncology).

Keywords

DNA methylation | primary CNS lymphoma | radiomics | risk score | survival

Funding

This work was funded by the Anniversary fund of the Austrian National Bank under [grant #16725 to A.W.], Austrian Science Fund [FWF #TAI98-B to A.W. and #P35189-B], the Vienna Science and Technology Fund [(WWTF) grants # LS20-034 to A.W. and # LS20-065 [10.47379/LS20065] to G.L], and the European Union's Horizon Europe research and innovation programme under grant agreement [#101100633-EUCAIM to G.L.]. The funders played no role in study design, data collection, analysis, and interpretation of data, or the writing of this manuscript.

Acknowledgments

The authors thank Johannes A. Hainfellner, Romana Hoeftberger, and Lisa Greutter, Division of Neuropathology and Neurochemistry at the Medical University of Vienna, for constructive discussions.

Conflict of interest statement

M.P. has received honoraria for lectures, consultation, or advisory board participation from the following for-profit companies: Bayer, Bristol-Myers Squibb, Novartis, Gerson Lehrman Group (GLG), CMC Contrast, GlaxoSmithKline, Mundipharma, Roche, BMJ Journals, MedMedia, Astra Zeneca, AbbVie, Lilly, Medahead, Daiichi Sankyo, Sanofi, Merck Sharp & Dome, Tocagen, Adastra, Gan & Lee Pharmaceuticals, but declares no nonfinancial competing interests. G.L. holds shares in the company contextflow and has received honoraria for lectures from the following for-profit companies: Boehringer Ingelheim, Novartis, and declares no nonfinancial competing interests. All other authors declare no financial or nonfinancial conflicts of interest.

Authorship statement

Experimental design: A.W., C.B., K.H.N., and G.L. Implementation: K.H.N., J.G., J.F., I.S., G.L., C.B., and A.W. Establishing the clinical cohort: J.F., T.R.P., S.W.C., S.L.L., T.B.K., M.B., K.C., C.F., A.G.,

J.H., S.H., M.H., S.I., B.K., M.K., W.K., F.M., P.M., S.O., D.P., M.B., C.S., G.S., M.S., C.T., J.T., T.U., S.W., G.W., F.W., M.P., and D.H.N. Analysis and interpretation of the data: K.H.N., J.G., J.F., A.N., C.B., G.L., and A.W. with contributions from T.R.P., S.W.C., C.M., S.L.L., J.K., B.E., B.B., I.S.K., and D.H.N. All authors confirm that they had full access to all the data in the study and accept responsibility to submit for publication. Coauthors reflect diversity in background, career-stage, gender, geography, and race. K.H.N., A.W., C.B., and G.L. have verified the underlying data.

References

1. Ferreri AJ, Blay JY, Reni M, et al. Prognostic scoring system for primary CNS lymphomas: the international extranodal lymphoma study group experience. *J Clin Oncol.* 2003;21(2):266–272.
2. Abrey LE, Ben-Porat L, Panageas KS, et al. Primary central nervous system lymphoma: the memorial sloan-kettering cancer center prognostic model. *J Clin Oncol.* 2006;24(36):5711–5715.
3. Barajas RF, Politi LS, Anzalone N, et al. Consensus recommendations for MRI and PET imaging of primary central nervous system lymphoma: guideline statement from the International Primary CNS Lymphoma Collaborative Group (IPCG). *Neuro Oncol.* 2021;23(7):1056–1071.
4. Lambin P, Leijenaar RTH, Deist TM, et al. Radiomics: the bridge between medical imaging and personalized medicine. *Nat Rev Clin Oncol.* 2017;14(12):749–762.
5. Schmitz R, Wright GW, Huang DW, et al. Genetics and pathogenesis of diffuse large B-cell lymphoma. *N Engl J Med.* 2018;378(15):1396–1407.
6. Chapuy B, Stewart C, Dunford AJ, et al. Molecular subtypes of diffuse large B cell lymphoma are associated with distinct pathogenic mechanisms and outcomes. *Nat Med.* 2018;24(5):679–690.
7. Nayyar N, White MD, Gill CM, et al. L265P mutation and loss are early mutational events in primary central nervous system diffuse large B-cell lymphomas. *Blood Adv.* 2019;3(3):375–383.
8. Camilleri-Broët S, Crinière E, Broët P, et al. A uniform activated B-cell-like immunophenotype might explain the poor prognosis of primary central nervous system lymphomas: analysis of 83 cases. *Blood.* 2006;107(1):190–196.
9. Radke J, Ishaque N, Koll R, et al. The genomic and transcriptional landscape of primary central nervous system lymphoma. *Nat Commun.* 2022;13(1):1–20.
10. Richter J, Ammerpohl O, Martín-Subero JI, et al. Array-based DNA methylation profiling of primary lymphomas of the central nervous system. *BMC Cancer.* 2009;9(1):1–8.
11. Nakamura T, Yamashita S, Fukumura K, et al. Genome-wide DNA methylation profiling identifies primary central nervous system lymphoma as a distinct entity different from systemic diffuse large B-cell lymphoma. *Acta Neuropathol.* 2017;133(2):321–324.
12. Vogt J, Wagener R, Montesinos-Rongen M, et al. Array-based profiling of the lymphoma cell DNA methylome does not unequivocally distinguish primary lymphomas of the central nervous system from non-CNS diffuse large B-cell lymphomas. *Genes Chromosomes Cancer.* 2019;58(1):66–69.
13. Downs BM, Ding W, Cope LM, et al. Methylated markers accurately distinguish primary central nervous system lymphomas (PCNSL) from other CNS tumors. *Clin Epigenetics.* 2021;13(1):104.
14. Landau DA, Clement K, Ziller MJ, et al. Locally disordered methylation forms the basis of intratumor methylome variation in chronic lymphocytic leukemia. *Cancer Cell.* 2014;26(6):813–825.
15. Pan H, Renaud L, Chaligne R, et al. Discovery of candidate DNA methylation cancer driver genes. *Cancer Discov.* 2021;11(9):2266–2281.
16. Shaknovich R, Geng H, Johnson NA, et al. DNA methylation signatures define molecular subtypes of diffuse large B-cell lymphoma. *Blood.* 2010;116(20):e81–e89.
17. Gaiti F, Chaligne R, Gu H, et al. Epigenetic evolution and lineage histories of chronic lymphocytic leukaemia. *Nature.* 2019;569(7757):576–580.
18. Chambwe N, Kormaksson M, Geng H, et al. Variability in DNA methylation defines novel epigenetic subgroups of DLBCL associated with different clinical outcomes. *Blood.* 2014;123(11):1699–1708.
19. Pan H, Jiang Y, Boi M, et al. Epigenomic evolution in diffuse large B-cell lymphomas. *Nat Commun.* 2015;6(1):1–12.
20. Hernández-Verdin I, Kirasic E, Wienand K, et al. Molecular and clinical diversity in primary central nervous system lymphoma. *Ann Oncol.* 2023;34(2):186–199.
21. Neuhauser M, Roetzer T, Oberndorfer S, et al. Increasing use of immunotherapy and prolonged survival among younger patients with primary CNS lymphoma: a population-based study. *Acta Oncol.* 2019;58(7):967–976.
22. Roetzer T, Furtner J, Gesperger J, et al. Sex-specific differences in primary CNS lymphoma. *Cancers* 2020;12(6):1593.
23. Lin X, Khan IRA, Seet YHC, Lee HY, Yu WY. Atypical radiological findings of primary central nervous system lymphoma. *Neuroradiology.* 2020;62(6):669–676.
24. Erdag N, Bhorade RM, Alberico RA, Yousuf N, Patel MR. Primary lymphoma of the central nervous system: typical and atypical CT and MR imaging appearances. *Am J Roentgenol.* 2001;176(5):1319–1326.
25. Tang YZ, Booth TC, Bhogal P, Malhotra A, Wilhelm T. Imaging of primary central nervous system lymphoma. *Clin Radiol.* 2011;66(8):768–777.
26. Jiménez de la Peña MD, Vicente LG, Alonso RC, et al. The multiple faces of nervous system lymphoma atypical magnetic resonance imaging features and contribution of the advanced imaging. *Curr Probl Diagn Radiol.* 2017;46(2):136–145.
27. Hans CP, Weisenburger DD, Greiner TC, et al. Confirmation of the molecular classification of diffuse large B-cell lymphoma by immunohistochemistry using a tissue microarray. *Blood.* 2004;103(1):275–282.
28. van Griethuysen JJM, Fedorov A, Parmar C, et al. Computational radiomics system to decode the radiographic phenotype. *Cancer Res.* 2017;77(21):e104–e107.
29. Friedman J, Hastie T, Tibshirani R. Regularization paths for generalized linear models via coordinate descent. *J Stat Softw.* 2010;33(1):1–22. https://pubmed.ncbi.nlm.nih.gov/20808728/. Accessed November 29, 2022.
30. Müller F, Scherer M, Assenov Y, et al. RnBeads 20: comprehensive analysis of DNA methylation data. *Genome Biol.* 2019;20(1):55.
31. Sheffield NC, Bock C. LOLA: enrichment analysis for genomic region sets and regulatory elements in R and Bioconductor. *Bioinformatics.* 2016;32(4):587–589.
32. Yin Y, Morgunova E, Jolma A, et al. Impact of cytosine methylation on DNA binding specificities of human transcription factors. *Science.* 2017;356(6337):eaaj2239.
33. Suh HB, Choi YS, Bae S, et al. Primary central nervous system lymphoma and atypical glioblastoma: differentiation using radiomics approach. *Eur Radiol.* 2018;28(9):3832–3839.
34. Kang KM, Choi SH, Chul-Kee P, et al. Differentiation between glioblastoma and primary CNS lymphoma: application of DCE-MRI parameters based on arterial input function obtained from DSC-MRI. *Eur Radiol.* 2021;31(12):9098–9109.
35. Priya S, Ward C, Locke T, et al. Glioblastoma and primary central nervous system lymphoma: differentiation using MRI derived first-order texture analysis - a machine learning study. *Neuroradiol J.* 2021;34(4):320–328.
36. Kunimatsu A, Kunimatsu N, Kamiya K, et al. Comparison between glioblastoma and primary central nervous system lymphoma using MR image-based texture analysis. *Magn Reson Med Sci.* 2018;17(1):50–57.

37. Kunimatsu A, Kunimatsu N, Yasaka K, et al. Machine learning-based texture analysis of contrast-enhanced MR imaging to differentiate between glioblastoma and primary central nervous system lymphoma. *Magn Reson Med Sci*. 2019;18(1):44–52.
38. Chen C, Zhuo H, Wei X, Ma X. Contrast-enhanced MRI texture parameters as potential prognostic factors for primary central nervous system lymphoma patients receiving high-dose methotrexate-based chemotherapy. *Contrast Media Mol Imaging*. 2019;2019:5481491.
39. Kim Y, Cho HH, Kim ST, et al. Radiomics features to distinguish glioblastoma from primary central nervous system lymphoma on multiparametric MRI. *Neuroradiology*. 2018;60(12):1297–1305.
40. Shur JD, Doran SJ, Kumar S, et al. Radiomics in oncology: a practical guide. *Radiographics*. 2021;41(6):1717–1732.
41. Napel S, Mu W, Jardim-Perassi BV, Hjwl A, Gillies RJ. Quantitative imaging of cancer in the postgenomic era: radio(geno)mics, deep learning, and habitats. *Cancer*. 2018;124(24):4633–4649.
42. Destito M, Marzullo A, Leone R, et al. Radiomics-based machine learning model for predicting overall and progression-free survival in rare cancer: a case study for primary CNS lymphoma patients. *Bioengineering (Basel)*. 2023;10(3):285.
43. Kreher S, Jöhrens K, Strehlow F, et al. Prognostic impact of B-cell lymphoma 6 in primary CNS lymphoma. *Neuro Oncol*. 2015;17(7):1016–1021.
44. Ge L, Lu S, Xu L, Yan H. MYC, BCL2, and BCL6 expression as prognostic indicators in primary central nervous system lymphoma: a systematic review and meta-analysis. *Clin Neurol Neurosurg*. 2021;208:106838.
45. Cardenas MG, Yu W, Beguelin W, et al. Rationally designed BCL6 inhibitors target activated B cell diffuse large B cell lymphoma. *J Clin Invest*. 2016;126(9):3351–3362.
46. Gao Y, Wei L, Kim SJ, et al. A novel prognostic marker for primary CNS lymphoma: lactate dehydrogenase-to-lymphocyte ratio improves stratification of patients within the low and intermediate MSKCC risk groups. *Front Oncol*. 2021;11:696147.